Sensing and Bio-Sensing Research 27 (2020) 100322

Contents lists available at ScienceDirect

Sensing and Bio-Sensing Research

journal homepage: www.elsevier.com/locate/sbsr

Coverage degrees of colloids on electrochemical electrodes and signal amplification for anti-citrullinated peptide antibody detection

Thanh T. Vu[a], Sojin Song[b], Hien D.N. Lai[c], Ngoc Lan Mai[a], Thuat T. Trinh[a,d], Ha T. Do[a], Dai Phu- Huynh[e,f], Anh H. Nguyen[a,*]

[a] Faculty of Applied Sciences, Ton Duc Thang University, 19 Nguyen Huu Tho Str., Tan Phong Ward, District 7, Ho Chi Minh City, Viet Nam
[b] Department of Chemical and Biological Engineering, Korea University, Seoul 136-713, South Korea
[c] Electronic Engineering Department, Kyunghee University, Yongin 17104, South Korea
[d] Department of Civil- and Environmental Engineering, Norwegian University of Science and Technology, 7491 Trondheim, Norway
[e] Faculty of Materials Technology, Ho Chi Minh City University of Technology, VNU – HCM, Viet Nam.
[f] Polymer research Center, Ho Chi Minh City University of Technology, VNU – HCM, Viet Nam.

ARTICLE INFO

Keywords:
Impedance biosensor
Rheumatoid arthritis
Cyclic citrullinated peptide
Label-free detection

ABSTRACT

Gold nanoparticles (AuNPs) have been used to increase the power of electrochemical biosensors. However, densities and pattern distributions of AuNPs colloids have not been determined yet. In this report, we attempt identifying coverable densities of AuNPs on interdigitated electrodes (IDEs) and increasing the sensing signal by using cyclic antigen (CCP)-coated-AuNPs in impedance biosensors. IDEs were covalently functionalized with CCP-coated AuNPs and used for detection of anti-CCP antibody (ACPA), a remarkable biomarker for rheumatoid arthritis. 36% and 82% of ACPA in human commercial serum were captured by a low CCP (300 CCP per 40-nm nanoparticles) and high CCP (17×10^5 CCP per 40-nm nanoparticles) densities of colloids, respectively. Coverage of the colloids on gaps between two digits of IDEs were observed about at 2.7×10^6 AuNPs (30 nm) per 1 μm^2 for low signal-to-noise ratio (SNR). The enzyme-catalyzed deposition of silver nanocrystal increased the SNR of the impedance signal up to 7.8 folds of magnitude higher than un-deposited counterparts. Sensitivity and limit of detection were determined at 1.3 ng/mL and 0.12 ng/mL, respectively, at a frequency 900 kHz in the range of 200–2000 kHz. Finally, Principal Component Analysis (PCA) showed the ability of the biosensor to follow variation over time of the number of CCP and therefore also the quantify of ACPA in the samples.

1. Introduction

Rheumatoid arthritis (RA) is an autoimmune disease in which mechanism relates to autoantibody production as a first stage to cause the synovial inflammation, cartilage, and bone destruction [1]. Therefore, autoantibodies are considered as potential biomarkers for the diagnostics of rheumatoid arthritis at early stages [2–4]. In terms of sensitivity and specificity, anti-citrullinated peptide antibody (ACPA) is an approved target for detection of rheumatoid arthritis (RA) in early stages [5–7]. The presence of ACPA forecasts persistent erosive disease and allows accurate prediction of RA, which has significant impact on the management of patients with early RA. The presence of ACPA provided a sensitivity of up to 67% with high specificity in the range of 94 to 97%, which showed that ACPA principally involves in RA development [5,8]. Although demand of point-of-care for RA in monitoring drug response and rehabilitation during treatment process has been available, it still has not developed in clinical settings due to lacking a miniaturized kit [9,10].

Currently, enzyme-linked immunosorbent assay (ELISA)-based method shows that ACPA against promiscuous cyclic citrullinated peptides (CCPs) has higher specificity, good predictive validity, and high sensitivity than RF for early stages [6,11]. Beside ELISA as a gold standard of the detection, updating assays for detection of ACPA and other antibodies have been developed by surface plasmon resonance (SPR) [12], localized surface plasmon resonance (LSPR) [13], surface-enhanced Raman scattered (SERS) [14,15], and electrochemical biosensors [16]. Although optical biosensors show high sensitivity with a limit of detection at picomolar regimes, they require more complex optical systems to collect and process the data, which significantly increase the cost of biosensors and narrow down their applicability. In addition, optical biosensors require extra steps of labeling probes with Raman and fluorescent dyes [17].

* Corresponding author.
E-mail address: nguyenhunganh@tdtu.edu.vn (A.H. Nguyen).

https://doi.org/10.1016/j.sbsr.2020.100322
Received 8 September 2019; Received in revised form 4 January 2020; Accepted 6 January 2020

Impedance-based biosensors on the platform of IDEs allow the potential of ease of miniaturization, label-free measurement, and low cost for point-of-care applications [18,19]. Previous studies reported derivate ELISA models can work well on IDEs with comprehensively different designs and surface modifications for many applications. These formats includes rapid detection of IFN-γ [20], DNA [21], metabolites [22], and hormone disorders [23–25]. When a biological target binds to a receptor-functionalized electrode, the dielectric properties, resistance, and impedance of electrodes are changed into new patterns. However, impedance biosensors have been reported that their performances show possible limitations for the detection, difficulties of miniaturizing AC impedance detection, noise signal from non-specific absorption on substrates, and how to make the reproducibility for biomolecule immobilization on the space of digit width of electrodes [26]. Incorporating AuNPs between electrode digits enhances the non-Faradaic impedance signal of IDEs due to a formation of the dielectric double layers between AuNPs and electrode surface, which amplify the sensitivity of the sensor [27]. This amplification relies on the density of the number of AuNPs in a nearby semiconductor and shows enhanced sensitivity at frequencies. In this case, the impedance of the biological layer itself was amplified by the response of field-effect sensor in conductance and capacitance under the effects of noble plasmonic nanoparticles [27–29].

Silver layer deposition has been widely used in the inverse sensitivity of plasmonic sensor [30] and in as a conducting bridge in organic materials for electronics [31]. The presence of silver nanoparticle (AgNPs) in polyaniline, a conductive polymer with an electric charge mechanism of single-and double conjugated bond hopping, influence the electrical properties [32]. However, for biomolecules such as protein, their electrical properties are shown as charge carriers whose hopping-type transport process that is directly driven by the nature of the protein-water interaction [33].

In this study, we identified densities and pattern distributions of AuNPs colloids onto IDEs, which support the increase of the conductivity. We attempt identifying coverable densities of AuNPs on IDEs and increasing the sensing signal by using cyclic antigen (CCP)-coated-AuNPs in impedance biosensors. IDEs were covalently functionalized with CCP-coated AuNPs and used for detection of anti-CCP antibody (ACPA), a remarkable biomarker for rheumatoid arthritis. The increased conductivity of the sensor is due to the electrical mobility derived from electron clouds of silver atoms in the space of digits. Gold IDEs (Dropsens, G-IDEAU5) with 5- μm digits between electrodes were used to detect ACPA in a microfluidic device. The microfluidics-based IDE biosensor promotes mass transport and reaction kinetics effects to increase the radial diffusion of biomolecules to each individual electrode. Limit of detection was determined at 0.12 ng/mL at 900 kHz in a frequency range of 200 kHz–2000 kHz. Finally, results showed that the deposition of silver nanocrystal increases the SNR of the impedance biosensor up to 7.8 folds of magnitude higher than undeposited counterparts. Due to higher mass transfer in a miniaturized scale device, detection of ACPA was reduced to 1 h for all steps. As a result, the device can be considered to further assessment to develop a point-of-care miniaturized device for rheumatoid arthritis detection.

2. Experimental

2.1. Reagents and apparatus

11-Mercaptoundecanoic acid (11-MUA), N-(3-(dimethylamino) propyl)-N′-ethylcarbodiimide hydrochloride (EDC), N-hydroxysuccinimide 98% (NHS), Anti-citrullinated peptide antibody (ACPA, ab6464, Abcam), and bovine serum albumin (BSA) were purchased from Sigma Aldrich. Sulfosuccinimidyl 4-(*N*-maleimidomethyl)-cyclohexane-1-carboxylate (sulfo SMCC) was from Thermo. Filaggrin-derived synthetic cyclic citrullinated peptides (CCP) were synthesized (Mimotopes, Australia). Ultrapure water (Milli-Q^R integral, Millipore, 18.2 mΩ. cm^{-1}) was used throughout the experiments. Ivium-Stat (10 μHz to 8 MHz, Ivium technologies, Netherlands) was used to measure the impedance spectroscopy. The interdigitated electrodes (IDE) were purchased from Dropsens (Ref. IDEAU5).

2.2. Functionalization of gold nanoparticles and interdigitated electrodes

AuNPs were synthesized by following the previous reports [34,35]. Briefly, 10 mL of 0.2 M CTAB in water and 0.μmL of 0.03 M $HAuCl_4$ in 1.0 mL of chilled 0.02 $NaBH_4$ were added in a reaction vial and reacted at 80 °C at high speed stirring (1300 rpm) for 10 min. The product was characterized using UV/Vis spectroscopy (UV-VIS, Cary 50, Varian) and high-resolution transmission electron microscopy (TEM) (JEM-2100F, 200 kV, JEOL). AuNPs were functionalized by ligand exchange with 11-MUA in a solution of 10% (*v*/v) Tween 20 in water in order to reduce aggregations for 8 h. 100 mM of CCPs were conjugated to the modified AuNPs through their side chain amine groups with carboxyl groups on the AuNPs under conjugation activation of EDC/NHS for 3 h. The resulting mixture was then centrifuged at 8000 rpm for 5 min and stored in 10 mM PBS added 0.02% Tween 20 for future use. The dynamic light scattering data reveals an increase in the hydrodynamic radius of the CCP coated AuNPs with the increase of surface coverage. The 50 μL of 10 mM modified AuNPs was dropped in channels between digit pairs in order to reduce their gaps and increase their dielectric characteristics. Unspecific binding sites on the sensor were blocked with 6% BSA solution in 10 mM PBS buffer for overnight.

Since CCPs are cyclic molecules with their side-chain lysine molecules, we used lysine-based conjugation for attaching CCP-AuNPs to IDEs. First, the IDEs were immersed in the freshly prepared 10 mM of 11-MUA in the absolute ethanol to form self-assembled monolayers for 30 min, resulting the carboxyl alkanethiol SAM on the IDEs. Any unbound molecules were removed by 70% ethanol. Subsequently, a simultaneous conjugation reaction was performed in 10 mM of MES buffer pH 6.0 with 5 mM of EDC, 5 mM of NHS, and 100 mM of CCP-coated AuNPs for 2 h at room temperature and then overnight at 4oC. Subsequently, the particles were purified by centrifugation three times with 12,000 rpm for 15 min [36]. The reaction occurs at the side-chain lysine-based conjugation with carboxylic acid terminated-group on the modified IDEs.

Method for conjugation of glucose oxidase (GOD) to anti-mouse IgG was conducted according to the previous study [30]. In the first tube, 2 mg of GOD in 1 mL of 10 mM PBS buffer (pH 7.4) was mixed with 250 μL of sulfo SMCC in water (3 mg/mL) for 1 h. In the second tube, 1 mg/mL of mouse polyclonal anti-human IgG in 10 mM PBS was reacted with 1.5 mg/mL 2-iminothiolane solution for 1 h at room temperature. Resulting products from tube 1 and tube 2 were purified with a P10 desalting column with PBS buffer. Protein (antibody)-rich fractions were monitored by their absorbance peak at 280 nm in a Nanodrop device. The last step was performed with a click-chemistry reaction between the thiol-modified antibody and maleimide-GOD for 1 h at room temperature in order to form a heterobifunctional linker. The final products were stored at 4 °C for future use.

2.3. Sensor setup and amplification of impedance signal

A polydimethylsiloxane (PDMS) microfluidics chip was mounted on IDEs sensor to form a reaction chamber. The as-prepared IDEs was incubated with 60 μL of various concentrations (2 ng to 78.1 ng) of ACPA spiked in human commercial serum (H4522, Sigma Aldrich) for 20 min, followed by a wash of three times with 10 mM PBS containing 0.05% Tween 20 (pH 7.4). Subsequently, 60 μL of 1 mM anti-human IgG antibody conjugated with GODs in 10 mM PBS was added in the chamber and incubated for 15 min. Finally, unbound glucose oxidase-conjugated IgGs were washed with 10 mM PBS 0.05% Tween 20 and a mixture of 50 mM $AgNO_3$ and 100 mM glucose was subsequently added to generate hydrogen oxide that reduce silver nitrate to forming silver crystal

growth deposited in AuNPs on the sensor. The impedance signal was monitored in real-time for each step. Regarding specific binding, the sensor was evaluated with human serum albumin (HSA) which has been reported a high presence in rheumatoid arthritis patients. Before taking electrochemical impedance spectroscopy (EIS) measurement, the device was washed with 10 mM PBS containing 0.05% Tween 20 for removal of unspecific binding.

All EIS experiments were conducted in Metrohm DropSens InterDigitated Electrodes (IDEs) which are composed of two interdigitated electrodes with two connection tracks, made of same material, on a glass substrate was mounted on the bottom of a PDMS chamber. Before measurement, the electrodes were cleaned with 70% ethanol solution and dried under gently stream of N2. The experiments were carried out in a three-electrode system with Ag/AgCl as reference electrode, a platinum wire as a counter electrode, and the IDE as the working electrode that were connected to the potentiostat BioLogic SP 200 (Fig. S7.). The working electrode IDEs composes of the array two interdigitated electrodes of two connection digits with their internal gaps with dimensions L 22.8 × W 7.6 × H 0.7 mm. The data acquisition was performed with Bio Logic SP 200 impedance analyzer with Bio-Logic software for analyzing impedance data. A three electrode cell with an Ag/AgCl electrode (MW-2030, Basinc, USA) and a platinum (Pt) counter electrode (MW-4130, Basinc, USA) was used for all measurements. All electrodes were washed with DI water and dried overnight at room temperature. The EIS was measured in a pure PBS 10 mM solution. The frequency range used for the measurement was in the range of 200–2000 kHz with 20 frequencies and with a 10 mV a.c. voltage superimposed on a bias d.c. voltage. All measurements were performed, and corresponding signals were recorded in a Nyquist and Bode plot. The impedance change was calculated as the difference between the impedance measured before and after the APCA was captured onto the IDE with PBS (10 mM) as the blank.

3. Results and discussion

3.1. Characterization of cyclic citrullinated peptide-modified electrodes

The schematic representation of the functionalization of the interdigitated electrode sensors was shown in Fig. 1. CCPs were covalently attached to AuNPs through the carbodiimide bond between their amine groups and the carboxyl group of 11-MUA on AuNP surface. The surface modification not only improves the stability and biocompatibility of gold colloids, but also functionalizes the AuNP surface, which is facilely linked with CCPs. Fig. S1A show the UV absorption spectra of bare and functionalized AuNPs at 535.5 nm and 542 nm, respectively. 7.5-nm shift towards red region show that refractive index of the functionalized AuNPs was changed due to coated CCP molecules (Fig. S1A). The CCP-coated AuNPs have almost no changes in their absorption spectra when the colloids are in PBS buffer and the commercial serum. This result showed that CCP-coated AuNPs were stable in working buffers (Fig. S1B). The colloidal suspension was then placed on the electrode surface, where the colloids were stated at the channel between two digits of the electrode (Fig. 1A) and a real electrode was shown in Fig. 1B. To amplify the impedance signal, the glucose- oxidase- based catalysis was performed to reduce silver ions to form silver nanocrystals that deposited on the AuNPs to form direct electron transfer via gold nanoparticle conjugation (Fig. 1C) [30,37]. With such a modification, the platform brings two advantages, the first thing is that AuNPs reduced the width of the channel between two digits of the electrode, which increases the electrical impedance of the solution in the sensing chamber. The second thing is that silver nanocrystals at the detection step increase from the real signal from the noise signal, which enhances SNR in the output signal [38,39].

Stereo microscope (left) and AFM 3D (right) images of G-IDEPT5 IDE electrode with 5 μm bands/gaps (Dropsens) are shown in Fig. 2A. The surface of an electrode and show silicon surface structure around electrodes are shown in Fig. 2B and C, respectively. Morphology of CCP-coated AuNPs was used to place in the channel of two digits of the electrode (Fig. 2D). Different densities of AuNPs on channels of electrodes that influence on impedance signal are shown in Fig. 2E. Through electrostatic interactions, moreover, AuNPs on glass substrate increased surface areas and played as nanoseeds for silver nanocrystals growth and self-assembly [40]. Distribution of AuNPs between two digits of electrodes could get the aggregated clusters that cause the short circuit [41]. To monitor the sensing surface, measuring changes in capacitance with impedance spectroscopy of AuNPs binding in the gaps between the electrodes was performed. Binding events alter the electrical properties in the gap between two electrodes, where changes in gap conductivity correspond to changes in real impedance component $Zr(w)$ and changes in the gap capacitance correspond to changes in the imaginary impedance component $Zi(w)$ [42]:

$$Z_{j\omega} = \frac{U_{j\omega}}{I_{j\omega}} = Z_r(\omega) + j\, Z_i(\omega) \tag{1}$$

$$z = \frac{1}{j\omega C} \tag{2}$$

$$\omega = 2\,\pi f \tag{3}$$

where ω is radial frequency expressed in radians/s) and f is frequency expressed in hertz [18]. Capacitive impedance as a result of surface modification was shown in Fig. 2E. In the presence of colloids, gaps between two electrodes reduce and the thickness of the dielectric layer increases, which result in changes of the electrical field at the electrode interface. It is demonstrated that the AuNPs coating on the glass substrate between two electrodes contributes not only to increase binding surface but also increase dielectric characteristics of gaps between two electrodes [43].

To prevent unspecific binding to the silicon substrate of the IDE surface, sensors were exposed to BSA solution (1 mg/ mL) for 30 min. The sensors were then washed three times with 10 mM PBS 0.05% Tween 20 and equilibrated before adding the CCP-coated AuNP colloidal suspensions. The average hydrodynamic radius of bare AuNPs was 30 nm, increasing to 57 nm at higher CCP coverage (Fig. S2). Since CCP has no net charge, we did not use the ζ-potential to clarify the potential of AuNPs before and after the modification. By calculating the number of CCP before and after immobilization (http://molbiol.edu.ru/eng/scripts/01_04.html), the average number of immobilized CCP saturates at levels in the range between 200 × 10^2 CCP/AuNP. In the presence of APCP in samples, the resistance of the electrode surface was increased as a response of dielectric and capacitive changes, which is common in label-free detection in protein biomarkers. The analogous capacitive response to each step of surface modification is shown in Fig. 2F where a sensitive modulation in response to ACPA-AuNPs colloids and silver nanocrystals deposition were observed. The affinity between CCP and ACPA was detected by ELISA and Western blot (Fig. S3).

3.2. Calculation of coverage degree of CCP-coated AuNPs on interdigitated electrodes

We observed that the CCP-modified AuNPs absorption efficiency follows the adsorption isotherm:

$$S = a_m \omega_m N^{-1} \tag{4}$$

where a_m is the amount of AuNPs covering the electrode surface in a monolayer pattern; ω_m is the surface that is occupied by an AuNP in the monolayer; N is the total number of AuNPs. According to (2) and (4), $z = \frac{d}{j\omega\varepsilon\varepsilon_0 A}$ narrow-downing the gap between electrodes from 5 μm down to 50 nm, but by AuNPs increased the impedance of electrodes 7.8 folds

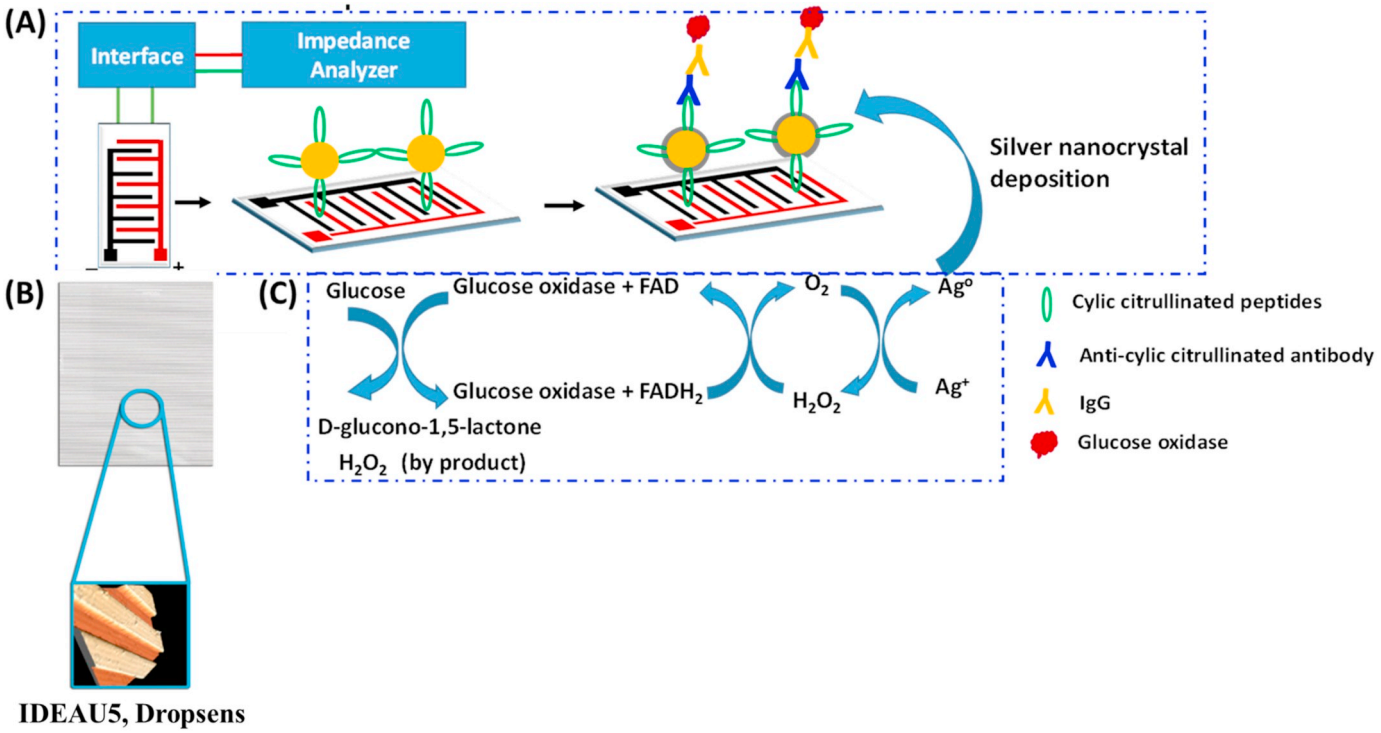

Fig. 1. Schematic illustration of interdigitated electrode biosensor fabrication. (A) Gold nanoparticles are conjugated with CCP and deposited on IDEs. ACPA as targets are bound to the CCP receptors and specifically detected by anti-human IgG molecules. GODs are conjugated to IgG to catalyze glucose to generate hydrogen peroxide in order to reduce Ag^{+} into Ag^{o} atoms to form Ag nanocrystal on surface of gold nanoparticle. (B) Geometry of IDEs (IDEAU5, Dropsens). (C) Mechanism of the GOD activity and enzyme-mediated silver nanocrystal reduction. (For interpretation of the references to colour in this figure legend, the reader is referred to the web version of this article.)

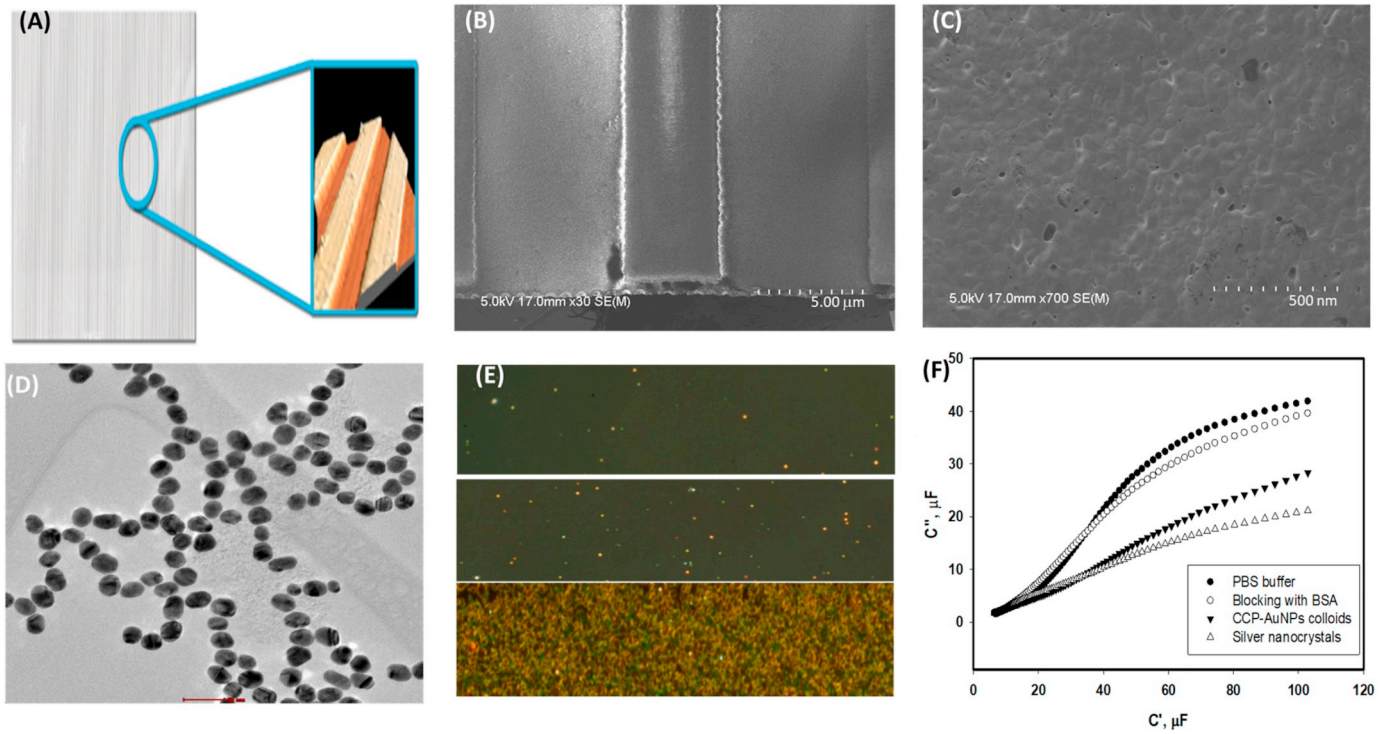

Fig. 2. Geometry and characterization of IDE. (A) Entire shape of IDEs. (B) SEM image of electrodes with 5 µm gaps between two digits. (C) Surface of IDEs for colloid distributions. (D) Gold nanoparticles for immuno colloidal bioconjugations. (E) Dark field images of gold nanoparticle distributions on IDEs. (F) Capacitive changes of IDES during modification processes from 40 µF to 15 µF corresponding to PBS and silver nanocrystal formation. (For interpretation of the references to colour in this figure legend, the reader is referred to the web version of this article.)

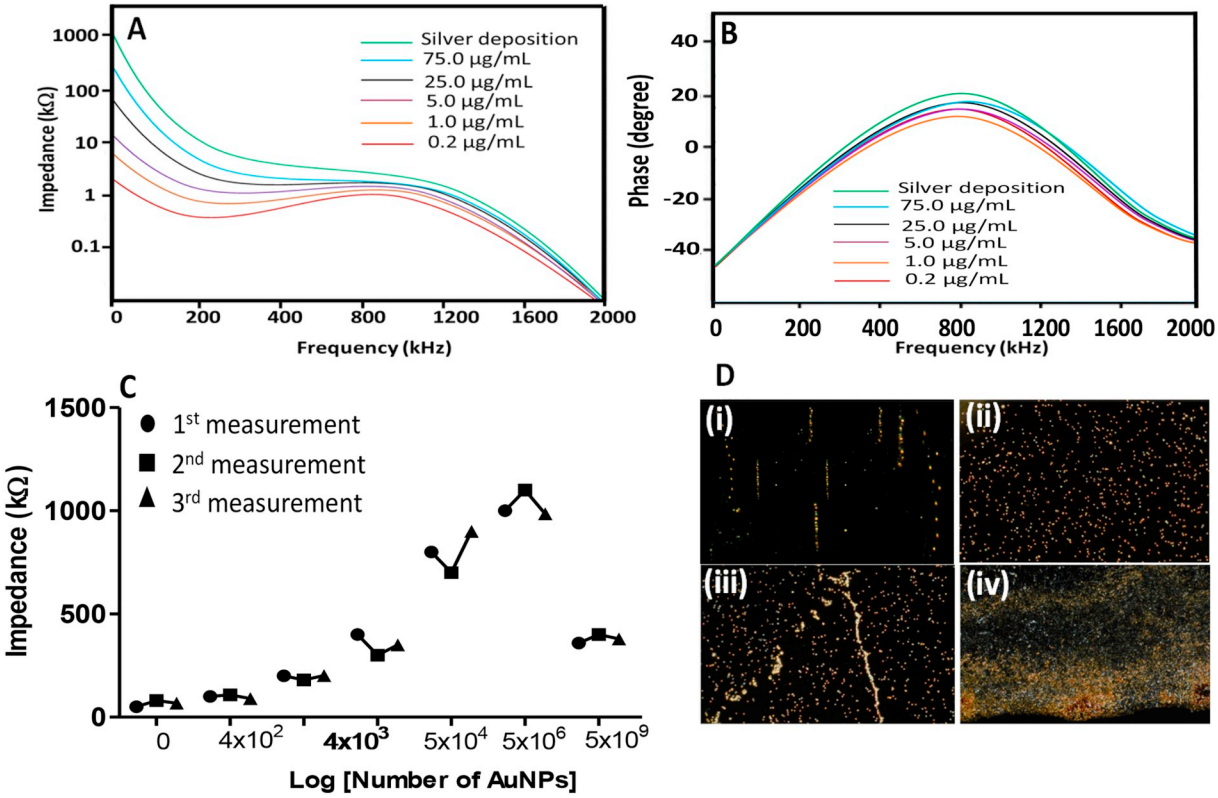

Fig. 3. Electrode bioconjugations and colloidal distributions. (A) Bode Plot with impedance against frequency (A) and phase degree against frequency (B) for different concentration of ACPA. The deposition of nanocrystal silver on gold colloids increases impedance in EIS. (C) Three measurements of colloidal distributions on IDEs. Number of colloids were highly affected impedance changes. (D) Dark field images of distributions of colloids. (i) PCR-based alignment of colloids in gaps between two digits of IDE. (ii) 4×10^3 colloids, (iii) 5×10^6 colloids, (iv) 5×10^9 colloids. (For interpretation of the references to colour in this figure legend, the reader is referred to the web version of this article.)

compared to that without using AuNPs and silver deposition. Fig. 3A-B shows the correlation between the impedance of the electrode and the density of AuNPs on electrodes. We plotted values of impedance as a function of frequency for CCP-coated AuNPs with their concentrations of 0.2 1, 5, 25, 75 μg/mL on the sensor. As shown in dielectric characteristics of gaps between two electrodes, the number of CCP-coated AuNPs on the sensor was proportional to impedance values with the frequency at 900 kHz.

We considered optimizing the sensor to detect the ACPA by evaluation of surface coverage of CCPs on AuNPs. The impedance of the IDEs increases with the added colloids in IDEs, over a wide surface coverage range of 5×10^4 to 5×10^9 colloids per 5 μm channel spaces. We note that the phenomena of short circuit occurred once the increased concentration of colloids up to 6×10^{10} per 5 μm channel spaces. Defective electrodes like electrically short-circuiting electrode pairs were observed because the circuit becomes a closed circuit that is not capable of generating electric fields to polarize colloids. Although a procedure of random distribution of colloids on electrode through the galvanostatic deposition is simple to increase the sensitivity of non-Faradaic EIS sensor, we found the increased impedance of biosensors did hardly match to the repeatability due to the random distribution of colloids on electrodes (Fig. 3C). Gold distributions on electrodes are shown in Fig. 3D where nanoparticles are aligned on polymerase chain reaction-based nanoparticle links [44] (Fig. 3D (i)) and random distributions with different concentrations of nanoparticles are shown in Fig. 3D (ii) to Fig. 3D (iv). In previous papers, the alignment of Ag nanoparticles by the external electrical field created by quadrupole electrode in refluxing condition [45]. Interestingly, a polymerase chain reaction occurs on the AuNPs surface that promoted end-by-end self-assembled alignment with controllable gaps between nanoparticles [44], which becomes useful for alignment of nanoparticles on IDE platform.

3.3. Determination of ACPA spiked in commercial human serum

The concentration of CCP used in the AuNP functionalization was ranged at 10, 50, 150, 300, 500 μg/mL and their results to the plasmonic change were shown in Fig. S4. Due to cyclic molecules, epitopes on AuNP surfaces are not affected by the steric hindrance. Given the dimension of AuNPs (40 nm) $V = \frac{4}{3}\pi R^3$=167.4 nm^3 and volume area of a channel 22.8×10^3 μm × 700 μm × 5 μm = 7.9×10^7 μm^3. We calculated a maximum AuNPs of 6.5×10^{10} AuNPs (50 nm) per channel to complete the coverage of the channel. Fig. 3C shows the concentration of AuNPs in range of 5×10^4–5×10^5 AuNPs (50 nm) per 1 μm^2 is an optimal working range to enhance the impedance signal. We note that the sensor was calibrated by 10 mM PBS to evaluate the influence of ionic strength on the impedance signal since the ionic strengths including hydrogen bonding, electrostatic interaction, dispersion forces, and hydrophobic interaction play an important role in the antibody-antigen interaction as a good model for a double layer for Nyquist plots analysis (Fig. 4A). In this case, Nyquist plots provided characteristics of a capacitance and a resistance in the parallel equivalent circuit. The circuit can be divided into three components: (i) the solution resistance Rs, between the CCP-coated AuNPs and the sensor surface, (ii) a resistance Rct and capacitance Cdl in parallel, corresponding to the antigen-antibody layer and the silver nanocrystal deposition on the surface, (iii) and Zw is Warburg impedance, corresponding to the molecular binding on the sensing surface [46]. Additional layers of silver on top of the CCP antigens increase the thickness of the molecular layer, which corresponds to the increase of the impedance (Fig. 4B).

The sensor was challenged with the commercial human plasma (and PBS to evaluate its efficiency. Before spiking, all human sera were tested for the presence of ACPA by ELISA, and all the samples

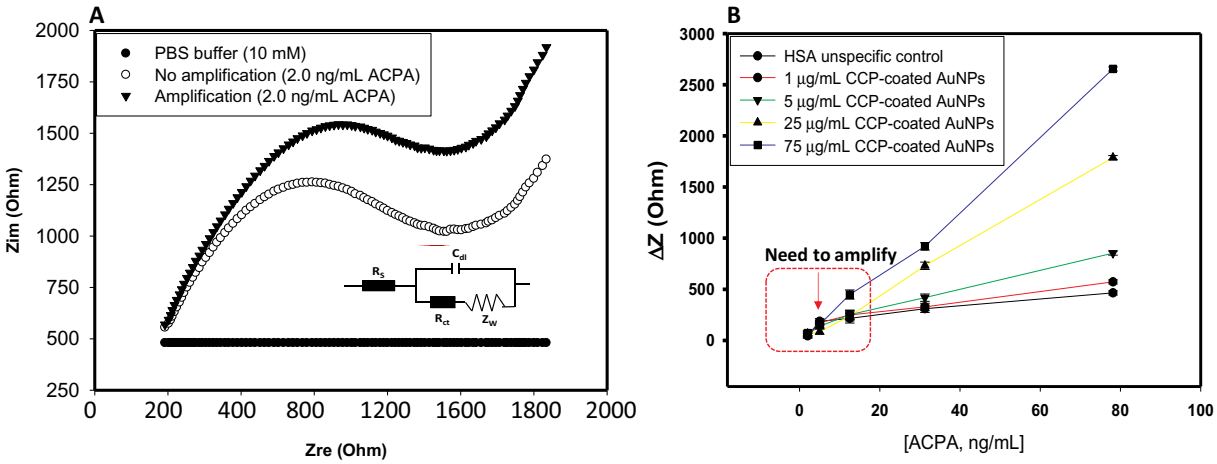

Fig. 4. Amplification of impedance signal via glucose oxidase-guided silver nanocrystal growth. (A) Nyquist plot was plotted in real and imaginary impedance for the amplification step. (B) Colloidal density-dependent impedance signal with a need of amplification for low concentrations of ACPA.

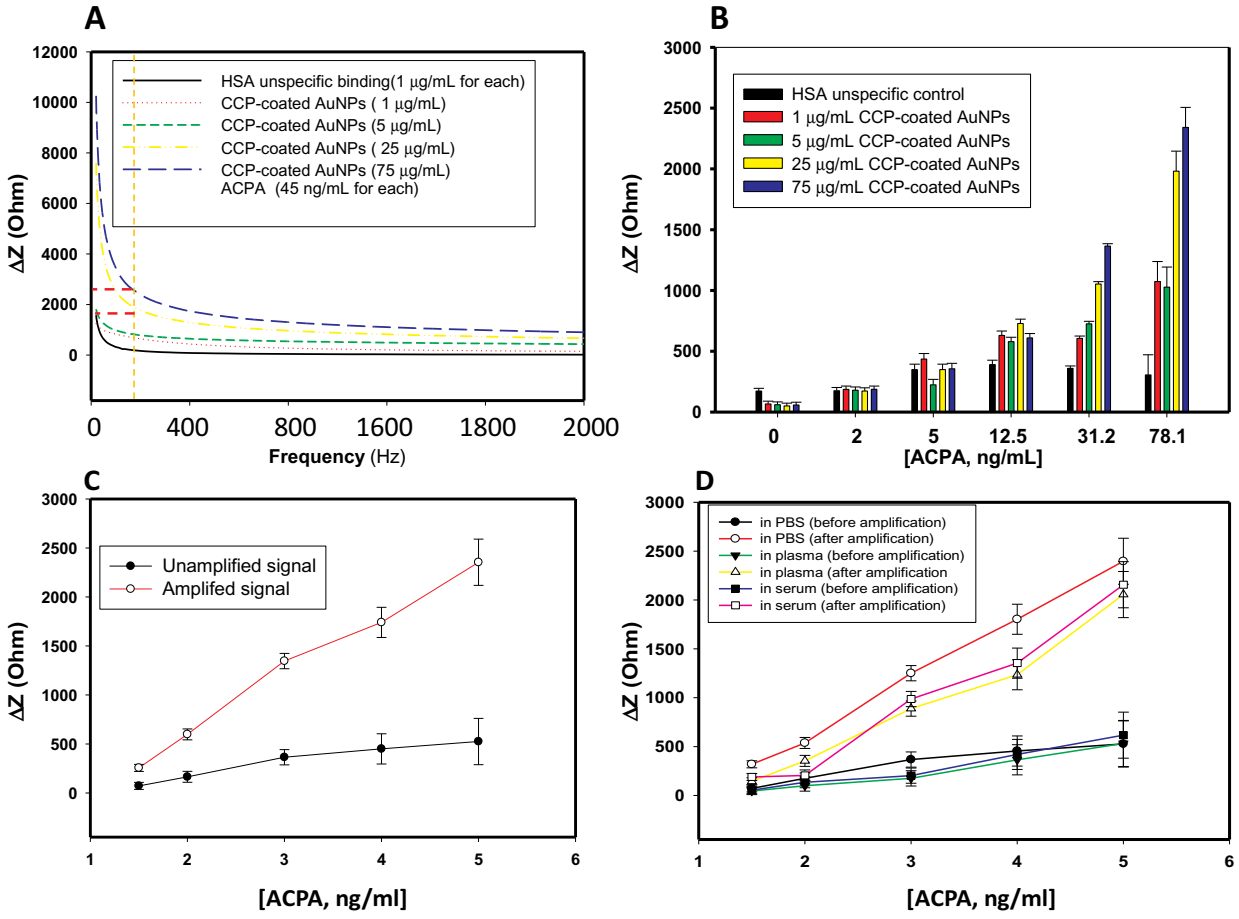

Fig. 5. Correlation between AuNPs density and ACPA concentration. (A) Bode plot of a single IDE electrode when it challenged to different concentration CCP-coated AuNPs. (B) Correlation between impedance and different concentrations of ACPA with different density of CCP-coated AuNPs. (C) Impedance increases 7.3 times after amplification with ACPA in PBS buffer. (B) Amplification with ACPA-spiked samples. Error bars represent the standard deviation, ± 2σ, of three consecutive EIS measurement on a single electrode. Before exposure to the target, the IDE electrode was sunk in PBS buffer until an equilibration signal was achieved.

were negative. We spiked two different concentrations of ACPA, 2 and 5 ng/mL as the critical range in the commercial serum sample. It has been previously reported that about cut-off 20 U/mL (3.2 ng/mL) or higher would be the critical concentration of the ACPA that, if detected in the serum samples, would refer to rheumatoid arthritis. For all experiments with commercial serum samples, the sensors were coated with 75 µg/mL of CCP-coated AuNPs to get the coverage of the sensor surface. The standard deviation (S.D) was received from three times of experiment. As shown in Fig. 5A, the sensor showed a robust specificity towards multiple ACPA concentrations in comparison with HSA as the unspecific control, where the sensors expressed a minimal response to the unspecific controls. The

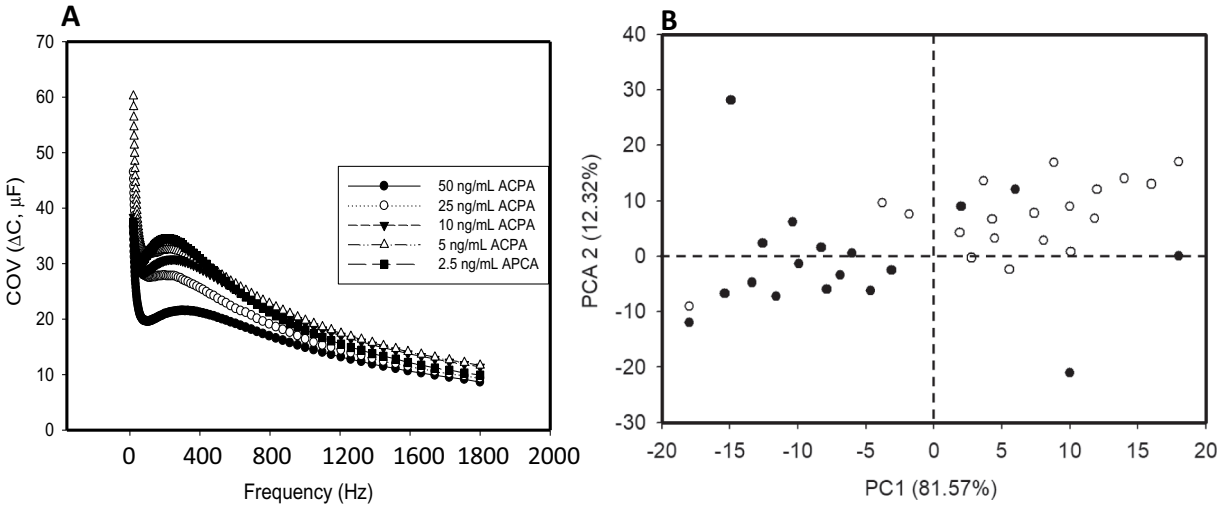

Fig. 6. Stability and reproducibility of electrochemical sensor with different physical treatments. (A) Calibration plot and corresponding coefficient of variation (COV), described as the relative standard deviation for the measurement on three different IDE electrodes, of ΔC versus frequency plot for each ACPA. Capacitance data for different ACPA concentrations to the sensor are fitted to the Hill eq. (B) Principal component analysis (PCA). PCA1 against PCA2 in terms of scores of normalized impedance intensity of samples. To normalize data, maximum background intensity was used and mean centered before doing PCA analysis. Plots of score from 19 impedance values of samples with different time of storage.

impedance magnitude is as a linear function of the concentration of the spiked ACPA in the human commercial serum and dramatically increased after the enzyme-mediated amplification. The slopes were increased from 130 to 603 (R^2 = 0.99), 139 to 525 (R^2 = 0.97), and 157 to 571 (R^2 = 0.97) Ohm. $(ng/mL)^{-1}$ for before- and after amplification corresponding to PBS, human commercial serum, and plasma, respectively with 13.7% S.D. for impedance.

The recording signal of ACPA concentration from 1 to 5 ng/mL was amplified by the enzyme-mediated amplification of signal in rea- time according to the GOD activity (Fig. 5B). GODs catalyze glucose molecules to generate H_2O_2 that reduces Ag^+ to Ag^o for the deposition, which enhances the recording signal. This effect is due to the hybridization of the dielectric constant of silver layers coated on gold nanoparticles. This experiment demonstrates that the silver deposition on the sensor is responsible for disrupting the electric field between electrodes, observing a change in impedance, forming hotspot sites in favor of either nucleation or the growth of silver nanocrystals. Based on the mechanism of impedance signal amplification by means of glucose oxidase-guided nanocrystal formation [47], we optimized the time of signal response by optimization of enzyme concentration.

3.4. Detection limit and signal-to-noise ratio

ACPA concentrations are at 1, 5, 25, and 75 ng/mL on sensors, as shown in Fig. 5C. The sensitivity of the sensor was determined by the amplified impedance signal at the frequency of 900 kHz for each concentration of ACPA in the range of ACPA concentration. The slope increased from 17 to 33, 67, 113, and 206 Ohm. $(ng/mL)^{-1}$ corresponding to 1 to 5, 25, and 75 ng/mL, respectively. The sensitivity of the sensor towards ACPA increased about two folds by doubling the concentration of the CCP-coated AuNPs. The detection range of the sensor highly depends on the concentration of CCP-coated AuNPs used in the coating step. At low concentrations of CCP-coated AuNPs, the impedance value showed a stationary curve. While, at higher concentration (25 and 75 μg/mL) of CCP-coated AuNPs, the sensor showed a considerable increase. As the density of CCP-coated AuNP increased on the sensor surface, it increased the density of the CCP receptors, and finally increased the yield of ACPA detection. This approach results in the enhancement of the detection limit (LOD) in which formula is defined as

$$LOD = \frac{3\,x\,SD_{blank}}{S}$$

where SD is the standard deviation of the blank and S is the of the regression line.

We calculated the LOD of the sensor at the CCP-coated AuNPs of 75 μg/mL with the used range of ACPA concentration from 2 to 78.1 ng/mL. The slope from the linear regression curve was 206 Ohm. $(ng/mL)^{-1}$ and the standard deviation of the blank was 82.4 Ohm. The LOD value was determined at 0.12 ng/mL. However, LOD values at each set of sensing assays showed a gentle variation with a percent of standard deviation at 21.3%, exception for 1 μg/mL of CCP-coated AuNPs (46.5% SD), which showed the variation in degree of correlation of LOD for each set of the experiment (Fig. 5C, D). On the other hand, the impedance magnitude was linearly increased in the concentration range of ACPA from 2.0 to 78.1 μg/mL. The result pointed out the threshold of the saturated density of CCP receptors on the sensor, which determined an effective and specific binding to ACPA. Moreover, coating the sensor with CCP-coated AuNPs, ACPA molecules bind to CCP at low steric hindrance due to cyclic structures of CCP. This would reduce an unspecific binding of matters in the complex serum to the sensor, which could open the usage of the sensor. Several previous studies reported that CCP receptors were used to make ELISA assay in clinical settings [1].

Nonspecific binding was well eliminated by BSA blocking (1 μg/mL) of the biosensor. Since HSA abundantly presents in the RA patient's sera, it was used as a negative control to compare with the targets for the impedance response in order to ensure the specificity of ACPA. Therefore, nonspecific is attributed to electrostatic interactions and slight binding affinity of ACPA and HSA. 60 μL of 1 μg/mL HSA generated a slight shift of 78 Ω (black column, Fig. 5D). A signal-to-noise ratio (S/N) was calculated by $SNR = 10 * \log\frac{Z_{signal}}{Z_{noise}}$ at each frequency with three measurements. The SNR values of ACPA at 25 ng/mL and HSA at 1 μg/mL were determined by 35.6 and 4.0, respectively, which indicates that the sensor is specific for the ACPA.

3.5. Reproducibility of biosensor

The sensing of the ACPA using CCP-modified sensors showed high stability and reproducibility as are shown in the coefficient-of-variation (COV) and principal component analysis (PCA) [48–50], respectively.

The COV of the stability of 5 samples over two months were between 11% to 16% (Fig. 6A). PCAs have figured out the obtained data from the samples in order to assess the reproducibility of the sensor. PCA analyses showed a high percentage of the total variant phase peaks (> 80%) being explained just with the first two principal components for all the time storages and different conditions. The PCA was used to identify the real impedance, capacitance, phase shift, and possible outliers. The result of PCA indicated that the highest variation related to increased resistance which is the proportional concentration of glucose oxidase. We note that PCA models were calculated using the truncated frequency distribution [51] for all the three single parameters of impedance, capacitance, and phase shift, respectively. First principal component (PC1) versus second principal component (PC2) presented a clustered distribution of the groups of different parameters in the frequency range between 200 kHz to 2000 kHz, which were performed in OriginPro 8.6. The first two PC was used to describe the total explained variances equaling to 93.89%, whereas PC1 and PC2 account for 81.57% and 12.32%, respectively (Fig. 6B).

It is possible to determine two different trends of time for the biosensor. First 17 samples (7 days) are characterized by descending scores along with PC2 axis, while the other samples (14 days) are distributed fundamentally along PC1 ascending scores related to aggregations of colloids. The distance between points was not changed as a function of treatment time that goes on and it can be explained by the stability of sensor surface (Fig. 6A). Indeed, the degradation of the biosensor is characterized by one of the incidents: (i) receptor degradation from the surface due to chemical, physical, or microbiological factors, (ii) reduction of real signal and increasing unspecific binding. In PCA, the reduction step corresponds to the 3 points that move along with PC2 axis, other samples correspond to along PC1 axis. Instead, unspecific samples assume lower scores along both PCs axes with increasing binding time. It is due to the low rate of binding or physically unspecific absorption during the sensing process.

4. Conclusion

A point-of-care device was fabricated for rapid detection of ACPA, an approved specific biomarker for RA, on an IDE platform. Although AuNPs have been used for increasing the sensitivity of the non-Faradaic electrochemical impedance, there is no report about at which concentrations are the optimal density for EIS on IDEs. Our results determined that the range of 5×10^4–5×10^5 AuNPs (50 nm) per 1 μm^2 is an optimal working range to enhance the impedance signal. The previous clinical studies showed that the presence of ACPA in the patient's sera at a concentration of ≥5 U/mL [52] or higher is critical biosignature of the RA. Our results determined the sensitivity of ACPA down to 1.3 ng/mL and LOD 0.12 ng/mL. Due to upon changes of impedance, the biosensor showed a faster response time of < 1 h and higher sensitivity due to the operation at small volumes. Such a device will make rapid bedside monitoring feasible with the goal of early detection of rheumatoid arthritis.

Declaration of Competing Interest

The authors declare no competing financial interest.

Acknowledgements

This research is funded by Vietnam National Foundation for Science and Technology Development (NAFOSTED) under grant number 108.06-2017.24.

Appendix A. Supplementary data

Supplementary data to this article can be found online at https://doi.org/10.1016/j.sbsr.2020.100322.

References

[1] I.B. McInnes, G. Schett, Pathogenetic insights from the treatment of rheumatoid arthritis, Lancet 389 (2017) 2328–2337.
[2] Y.W. Song, E.H. Kang, Autoantibodies in rheumatoid arthritis: rheumatoid factors and anticitrullinated protein antibodies, QJM 103 (2010) 139–146.
[3] S. Bugatti, A. Manzo, C. Montecucco, R. Caporali, The clinical value of autoantibodies in rheumatoid arthritis, Front. Med. 5 (2018) 339.
[4] S. de Brito Rocha, D.C. Baldo, L.E.C. Andrade, Clinical and pathophysiologic relevance of autoantibodies in rheumatoid arthritis, Adv. Rheumatol. 59 (2019) 2 2019/01/17.
[5] R. Aggarwal, K. Liao, R. Nair, S. Ringold, K.H. Costenbader, Anti-citrullinated peptide antibody assays and their role in the diagnosis of rheumatoid arthritis, Arthritis Rheum. 61 (2009) 1472–1483.
[6] R. Toes, D.S. Pisetsky, Pathogenic effector functions of ACPA: where do we stand? Ann. Rheum. Dis. 78 (2019) 716.
[7] N.H. Trier, B.E. Holm, P.R. Hansen, O. Slot, H. Locht, G. Houen, Specificity of anti-Citrullinated protein antibodies in rheumatoid arthritis, Antibodies (Basel, Switzerland) 8 (2019) 37.
[8] G.J.M. Pruijn, A. Wiik, W.J. van Venrooij, The use of citrullinated peptides and proteins for the diagnosis of rheumatoid arthritis, Arthritis Res. Ther. 12 (2010) 203 2010/02/15.
[9] P. Rojanasantikul, P. Pattrapornpisut, K. Anuruckparadorn, W. Katchamart, The performance of a point of care test for detection of anti-mutated citrullinated vimentin and rheumatoid factor in early rheumatoid arthritis, Clin. Rheumatol. 33 (2014) 919–923 2014/07/01.
[10] K.N. Konstantinov, A. Tzamaloukas, R.L. Rubin, Detection of autoantibodies in a point-of-care rheumatology setting, Auto Immunity Highlights 4 (2013) 55–61.
[11] W.J. van Venrooij, J.J.B.C. van Beers, G.J.M. Pruijn, Anti-CCP antibodies: The past, the present and the future, Nat. Rev. Rheumatol. 7 (2011) 391 06/07/online.
[12] J.J.B.C. van Beers, A. Willemze, J.J. Jansen, G.H.M. Engbers, M. Salden, J. Raats, et al., ACPA fine-specificity profiles in early rheumatoid arthritis patients do not correlate with clinical features at baseline or with disease progression, Arthritis Res. Ther. 15 (2013) R140 2013/10/01.
[13] K.A. Willets, R.P. Van Duyne, Localized surface Plasmon resonance spectroscopy and sensing, Annu. Rev. Phys. Chem. 58 (2007) 267–297 2007/05/01.
[14] H. Chon, S. Lee, R. Wang, S.-Y. Bang, H.-S. Lee, S.-C. Bae, et al., SERS-based immunoassay of anti-cyclic citrullinated peptide for early diagnosis of rheumatoid arthritis, RSC Adv. 4 (2014) 32924–32927.
[15] A.H. Nguyen, Y. Shin, S.J. Sim, Development of SERS substrate using phage-based magnetic template for triplex assay in sepsis diagnosis, Biosens. Bioelectron. 85 (2016) 522–528 2016/11/15/.
[16] S. Campuzano, M. Pedrero, A. González-Cortés, P. Yáñez-Sedeño, J.M. Pingarrón, Electrochemical biosensors for autoantibodies in autoimmune and cancer diseases, Anal. Methods 11 (2019) 871–887.
[17] A.H. Nguyen, J. Lee, H. Il Choi, H. Seok Kwak, S. Jun Sim, Fabrication of plasmon length-based surface enhanced Raman scattering for multiplex detection on microfluidic device, Biosens. Bioelectron. 70 (2015) 358–365 2015/08/15/.
[18] J.S. Daniels, N. Pourmand, Label-free impedance biosensors: opportunities and challenges, Electroanalysis 19 (2007) 1239–1257.
[19] T. Bertok, L. Lorencova, E. Chocholova, E. Jane, A. Vikartovska, P. Kasak, et al., Electrochemical impedance spectroscopy based biosensors: Mechanistic principles, analytical examples and challenges towards commercialization for assays of protein Cancer biomarkers, ChemElectroChem 6 (2019) 989–1003 2019/02/15.
[20] S. Ding, C. Mosher, X.Y. Lee, S.R. Das, A.A. Cargill, X. Tang, et al., Rapid and label-free detection of interferon gamma via an electrochemical Aptasensor comprising a ternary surface monolayer on a gold interdigitated electrode Array, ACS Sensors 2 (2017) 210–217 2017/02/24.
[21] P. Quan Li, A. Piper, I. Schmueser, A.R. Mount, D.K. Corrigan, Impedimetric measurement of DNA–DNA hybridisation using microelectrodes with different radii for detection of methicillin resistant Staphylococcus aureus (MRSA), Analyst 142 (2017) 1946–1952.
[22] D. Butler, N. Goel, L. Goodnight, S. Tadigadapa, A. Ebrahimi, Detection of bacterial metabolism in lag-phase using impedance spectroscopy of agar-integrated 3D microelectrodes, Biosens. Bioelectron. 129 (2019) 269–276 2019/03/15/.
[23] S. Guo, T. Lakshmipriya, S.C.B. Gopinath, P. Anbu, Y. Feng, Complementation of ELISA and an interdigitated electrode surface in gold nanoparticle functionalization for effective detection of human blood clotting defects, Nanoscale Res. Lett. 14 (2019) 222.
[24] G.V. Soraya, J. Chan, T.C. Nguyen, D.H. Huynh, C.D. Abeyrathne, G. Chana, et al., An interdigitated electrode biosensor platform for rapid HLA-B*15:02 genotyping for prevention of drug hypersensitivity, Biosens. Bioelectron. 111 (2018) 174–183 2018/07/15/.
[25] M. Kim, R. Iezzi, B.S. Shim, D.C. Martin, Impedimetric biosensors for detecting vascular endothelial growth factor (VEGF) based on poly(3,4-ethylene dioxythiophene) (PEDOT)/gold nanoparticle (au NP) composites, Front. Chem. 7 (2019) 2019-April-16.
[26] R. Radhakrishnan, I.I. Suni, C.S. Bever, B.D. Hammock, Impedance biosensors: applications to sustainability and remaining technical challenges, ACS Sustain. Chem. Eng. 2 (2014) 1649–1655.
[27] K.V. Singh, D.K. Bhura, G. Nandamuri, A.M. Whited, D. Evans, J. King, et al., Nanoparticle-enhanced sensitivity of a Nanogap-interdigitated electrode Array Impedimetric biosensor, Langmuir 27 (2011) 13931–13939 2011/11/15.
[28] J. Lu, W. Wang, S. Wang, X. Shan, J. Li, N. Tao, Plasmonic-based electrochemical impedance spectroscopy: Application to molecular binding, Anal. Chem. 84 (2012)

327–333 2012/01/03.
[29] L. Yuan, N. Tao, W. Wang, Plasmonic imaging of electrochemical impedance, Annu. Rev. Anal. Chem. 10 (2017) 183–200 2017/06/12.
[30] L. Rodríguez-Lorenzo, R. de la Rica, R.A. Álvarez-Puebla, L.M. Liz-Marzán, M.M. Stevens, Plasmonic nanosensors with inverse sensitivity by means of enzyme-guided crystal growth, Nat. Mater. 11 (2012) 604 05/27/Online.
[31] T.E. Glier, L. Akinsinde, M. Paufler, F. Otto, M. Hashemi, L. Grote, et al., Functional printing of conductive silver-nanowire photopolymer composites, Sci. Rep. 9 (2019) 6465 2019/04/23.
[32] A. Choudhury, Polyaniline/silver nanocomposites: Dielectric properties and ethanol vapour sensitivity, Sensors Actuators B 138 (2009) 318–325 2009/04/24/.
[33] N.L. Ing, M.Y. El-Naggar, A.I. Hochbaum, Going the distance: Long-range conductivity in protein and peptide bioelectronic materials, J. Phys. Chem. B 122 (2018) 10403–10423 2018/11/21.
[34] A.H. Nguyen, S.J. Sim, Nanoplasmonic biosensor: Detection and amplification of dual bio-signatures of circulating tumor DNA, Biosens. Bioelectron. 67 (2015) 443–449 2015/05/15/.
[35] E.G. Wrigglesworth, J.H. Johnston, The use of dual reductants in gold nanoparticle syntheses, RSC Adv. 7 (2017) 45757–45762.
[36] D. Bartczak, A.G. Kanaras, Preparation of peptide-functionalized gold nanoparticles using one pot EDC/Sulfo-NHS coupling, Langmuir 27 (2011) 10119–10123 2011/08/16.
[37] J.T. Holland, C. Lau, S. Brozik, P. Atanassov, S. Banta, Engineering of glucose oxidase for direct Electron transfer via site-specific gold nanoparticle conjugation, J. Am. Chem. Soc. 133 (2011) 19262–19265 2011/12/07.
[38] A. Bonanni, M. Pumera, Y. Miyahara, Influence of gold nanoparticle size (2–50 nm) upon its electrochemical behavior: an electrochemical impedance spectroscopic and voltammetric study, Phys. Chem. Chem. Phys. 13 (2011) 4980–4986.
[39] K. Sun, Y. Chang, B. Zhou, X. Wang, L. Liu, Gold nanoparticles-based electrochemical method for the detection of protein kinase with a peptide-like inhibitor as the bioreceptor, Int. J. Nanomedicine 12 (2017) 1905–1915.
[40] B.A. Korgel, S. Fullam, S. Connolly, D. Fitzmaurice, Assembly and self-Organization of Silver Nanocrystal Superlattices: Ordered "soft spheres", J. Phys. Chem. B 102 (1998) 8379–8388 1998/10/01.
[41] S. Nadzirah, N. Azizah, U. Hashim, S.C.B. Gopinath, M. Kashif, Titanium dioxide nanoparticle-based interdigitated electrodes: a novel current to voltage DNA biosensor Recognizes E. coli O157:H7, PLoS ONE 10 (2015) e0139766.
[42] E. Katz, I. Willner, Probing biomolecular interactions at conductive and Semiconductive surfaces by impedance spectroscopy: Routes to Impedimetric Immunosensors, DNA-sensors, and enzyme biosensors, Electroanalysis 15 (2003) 913–947 2003/07/01.
[43] Y. Zhao, M. Wang, J. Yao, Characterization of colloidal particles using electrical impedance spectroscopy in two-electrode system with carbon probe, Procedia Engg. 102 (2015) 322–328 2015/01/01/.
[44] W. Ma, H. Kuang, L. Xu, L. Ding, C. Xu, L. Wang, et al., Attomolar DNA detection with chiral nanorod assemblies, Nat. Commun. 4 (2013) 2689 10/28/online.
[45] R. Gholipur, A. Bahari, Alignment of ag nanoparticles by an external electric field proposed for metamaterial applications, Curr. Appl. Phys. 17 (2017) 989–998 2017/07/01/.
[46] D.C. Kim, D.J. Kang, Molecular recognition and specific interactions for biosensing applications, Sensors (Basel, Switzerland) 8 (2008) 6605–6641.
[47] D. Liu, J. Yang, H.-F. Wang, Z. Wang, X. Huang, Z. Wang, et al., Glucose oxidase-catalyzed growth of gold nanoparticles enables quantitative detection of Attomolar Cancer biomarkers, Anal. Chem. 86 (2014) 5800–5806 2014/06/17.
[48] A.H. Nguyen, X. Ma, H.G. Park, S.J. Sim, Low-blinking SERS substrate for switchable detection of kanamycin, Sensors Actuators B Chem. 282 (2019) 765–773 2019/03/01.
[49] C. Conesa, E. García-Breijo, E. Loeff, L. Seguí, P. Fito, N. Laguarda-Miró, An electrochemical impedance spectroscopy-based technique to identify and quantify fermentable sugars in pineapple waste valorization for bioethanol production, Sensors (Basel, Switzerland) 15 (2015) 22941–22955.
[50] R. Bro, A.K. Smilde, Principal component analysis, Anal. Methods 6 (2014) 2812–2831.
[51] H. Shou, V. Zipunnikov, C.M. Crainiceanu, S. Greven, Structured functional principal component analysis, Biometrics 71 (2015) 247–257.
[52] B.J. Miriovsky, K. Michaud, G.M. Thiele, J.R. O'Dell, G.W. Cannon, G. Kerr, et al., Anti-CCP antibody and rheumatoid factor concentrations predict greater disease activity in men with rheumatoid arthritis, Ann. Rheum. Dis. 69 (2010) 1292–1297.

Anh H. Nguyen, Ton Duc Thang University.

BIOGRAPHICAL SKETCH

INSTITUTION AND LOCATION	DEGREE *(if applicable)*	START DATE MM/YYYY	END DATE MM/YYYY	FIELD OF STUDY
University of Sciences, Vietnam	Bachelor	09/1999	09/2003	Biotechnology
Sungkyungkwan University, Korea	Master	09/2007	09/2009	Medical Sciences
Transnational University of Limburg, Belgium	Master	09/2009	07/2011	Clinical Molecular Biology
Korea University, Korea	Ph.D.	09/2012	09/2016	Chemical and Biological Engineering (Surface-enhanced Raman scattering, opto/microfluidic chips)
Korea University, Korea	Postdoctoral Training	10/2016	3/2017	Surface-enhanced Raman scattering, opto/microfluidic chips
University of Alberta, Canada	Postdoctoral Training	4/2017	2/2019	Magnetic Nanoparticle-based gene delivery, Electrochemical Biosensor
University of California, Irvine	Project Scientist	2/2019	8/2019	Cardiac Tissue Engineering and Electrochemical biosensor
Ton Duc Thang University	Adjunct professor	1/2017	Present	Nano chemistry and Biosensor